

# MFF budding from mitochondria regulates melanosome size and maturation

Received: 24 June 2024

Accepted: 26 February 2026

Cite this article as: Magalhães Rebelo, A.P., Maracani, A., Greco, S. *et al.* MFF budding from mitochondria regulates melanosome size and maturation. *Nat Commun* (2026). <https://doi.org/10.1038/s41467-026-70572-3>

Ana Paula Magalhães Rebelo, Aurora Maracani, Samuele Greco, Federica Dal Bello, Lucia Santorelli, Marco Gerdol, Alberto Pallavicini, Tomas Knedlik, Sara Schiavon, Luca Scorrano, Philip S. Goff, Christian Frezza, Elena V. Sviderskaya, Paolo Grumati & Marta Giacomello

We are providing an unedited version of this manuscript to give early access to its findings. Before final publication, the manuscript will undergo further editing. Please note there may be errors present which affect the content, and all legal disclaimers apply.

If this paper is publishing under a Transparent Peer Review model then Peer Review reports will publish with the final article.

**TITLE: MFF budding from mitochondria regulates melanosome size and maturation**

**Authors:** Ana Paula Magalhães Rebelo<sup>1,2\*</sup>, Aurora Maracani<sup>1,3</sup>, Samuele Greco<sup>4</sup>, Federica Dal Bello<sup>1</sup>, Lucia Santorelli<sup>5</sup>, Marco Gerdol<sup>4</sup>, Alberto Pallavicini<sup>4</sup>, Tomas Knedlik<sup>1</sup>, Sara Schiavon<sup>1</sup>, Luca Scorrano<sup>1,3</sup>, Philip S. Goff<sup>6</sup>, Christian Frezza<sup>2,7</sup>, Elena V. Sviderskaya<sup>6</sup>, Paolo Grumati<sup>5,8</sup>, Marta Giacomello<sup>1\*</sup>

**Affiliations:**

<sup>1</sup>Department of Biology, University of Padova, Via U. Bassi 58/B, 35121 Padua, Italy

<sup>2</sup>Faculty of Medicine, University of Cologne, and University Hospital Cologne, Institute for Metabolomics in Ageing, Cluster of Excellence Cellular Stress Responses in Aging-associated Diseases (CECAD), Cologne, Germany.

<sup>3</sup>Veneto Institute of Molecular Medicine, 35129 Padova, Italy

<sup>4</sup>Department of Life Sciences, University of Trieste, Via Licio Giorgieri, 5 - 34127 Trieste, Italy

<sup>5</sup>Telethon Institute of Genetics and Medicine (TIGEM), Pozzuoli, Italy

<sup>6</sup>School of Health and Medical Sciences, City St George's, University of London, Cranmer Terrace, London SW17 0RE, UK

<sup>7</sup>Faculty of Mathematics and Natural Sciences, University of Cologne, Institute of Genetics, Cluster of Excellence Cellular Stress Responses in Aging-associated Diseases (CECAD), Cologne, Germany.

<sup>8</sup>Department of Clinical Medicine and Surgery, Federico II University, Naples, Italy

\*Corresponding author. Email: [marta.giacomello@unipd.it](mailto:marta.giacomello@unipd.it) and [amagalha@uni-koeln.de](mailto:amagalha@uni-koeln.de)

**ABSTRACT**

Melanosomes are lysosome-related organelles that produce and accumulate melanin. Their maturation is regulated through interactions with mitochondria and involves the export and recycling of proteins via tubular transport and fission events whose mechanisms are unknown. Here, we demonstrate that the mitochondrial fission factor protein (MFF) is involved in melanosome fission. MFF is trafficked between mitochondria and melanosomes and localizes at melanosome fission events. Upon downregulation of MFF, but not of dynamin-related protein 1, melanosomes enlarge, intracellular melanin accumulates, melanosomal luminal catabolism increases, indicating that MFF-dependent melanosome fission is required for their maturation. We show that MFF interacts with regulators of the ARP2/3 complex, which drives F-actin nucleation. Actin filaments accumulate between melanosomes at MFF-enriched membrane constriction sites, and silencing of ARP2/3 subunits mimicks the increase in melanosome size. MFF regulates actin-dependent fission of melanosomes via the ARP2/3 complex, indicating an extramitochondrial function for MFF in the regulation of melanosome homeostasis.

## INTRODUCTION

Lysosome-related organelles (LROs) are cell-type-specific organelles of endosomal and/or secretory origin that share adaptive physiological functions, morphological features, and cargoes. Pigmented cells such as epidermal melanocytes and retinal pigment epithelial cells contain melanosomes, a type of LRO that allows compartmentalization of synthesis and storage of melanin pigments <sup>1,2</sup>.

Melanosomes share several features with lysosomes. These include acidic intraluminal pH, the presence of lysosomal membrane proteins, luminal proteases, and hydrolases, including cathepsins <sup>3-5</sup>. Even so, melanosome identity is determined by the presence of specific melanogenesis-associated machinery, such as the pre-melanosome protein (GP100; also known as PMEL17), Tyrosinase (TYR), and Tyrosinase-related proteins 1 and 2 (TYRP1/TYRP2) <sup>6</sup>.

Melanosomes have been proposed to arise from endosomes and multivesicular bodies (MVBs). They are classified into four different stages of maturation based on distinct morphological features. Stage I melanosomes (pre-melanosomes or early melanosomes) are unpigmented

endosomal-like compartments lacking melanogenic enzymes and characterized by luminal membranous vesicles<sup>7</sup>. Stage II melanosomes exhibit an ellipsoidal shape with striae, due to the presence of GP100 that assembles into amyloidogenic fragments and then into parallel longitudinal fibers within the lumen of the organelle. Stage III melanosomes contain melanogenic enzymes like TYR and TYRP1/2 and visible melanin deposition onto GP100 scaffold/structured sheets. Stage IV melanosomes are fully pigmented and, under physiological conditions, move to the cell periphery where they are secreted and subsequently taken up by keratinocytes<sup>8,9</sup>.

The maturation of melanosomes occurs upon delivery/export of melanogenic proteins through the endolysosomal recycling pathway. In line with their endosomal lineage, melanosomes appear to have the plastic and dynamic capacity to undergo homotypic fusion and fission through tubular and/or vesicular membrane remodeling<sup>10-16</sup>.

This idea is supported by the evidence that myosin 6 (MYO6), along with optineurin (OPTN), Wiskott-Aldrich syndrome protein and SCAR homolog (WASH), and the actin-related protein 2/3 (ARP2/3)-dependent actin nucleation complex participate in melanosome membrane constriction and fission events<sup>15</sup>. Specifically, MYO6 mediates the severing of vesicle-associated membrane protein 7 (VAMP7)-positive tubule necks emerging from melanosome membrane subdomains. This process allows the export of non-essential components and fosters proper melanosome maturation<sup>15</sup>. Modulators of phosphatidylinositol 3,5-bisphosphate (PI(3,5)P<sub>2</sub>) levels, like the kinase PIKfyve, also promote the formation and release of membrane tubules from early melanosomes<sup>17</sup>. Therefore, it is likely that different types of machinery regulate melanosome membrane remodeling, depending on the maturation stage.

Mitochondria supply ATP and calcium (Ca<sup>2+</sup>) to support melanosome maturation and melanin synthesis<sup>18-20</sup>. Early-stage melanosomes have been shown to interact more with mitochondria<sup>19</sup>. Two possible explanations could account for this evidence. First, the proximity between organelles

could facilitate the entry of ATP into the melanosomes, thereby fostering melanin synthesis and their maturation; second, it could support the recruitment of specific mitochondrial proteins to the melanosome surface during melanogenesis. Which would be the case still needs to be clarified.

Mitochondria and melanosomes are physically in contact through the outer mitochondrial membrane (OMM) protein mitofusin 2 (MFN2) that regulates mitochondria-melanosome apposition in space and time during active melanogenesis<sup>19</sup>. Whether the communication between these two organelles extends beyond the established role of MFN2 is unknown, despite mounting evidence for the role of mitochondria contact sites in several cellular processes, like Ca<sup>2+</sup> homeostasis, lipid metabolism, and organelle function and dynamics.

While investigating the role of the mitochondrial proteome in melanosome function, we found that the mitochondrial fission factor (MFF) is present on the surface of melanosomes, independently of mitochondria. MFF localization on the melanosome surface enables it to interact with components of the ARP2/3 complex, facilitating early melanosome fission without its mitochondrial pro-fission partner DRP1. The promotion of Fmaturation, and for their function during melanogenesis.

## RESULTS

## **Comparison of pigmented and albino melanocytes identifies MFF involvement in mitochondria-melanosomes crosstalk**

To clarify the role of the interaction between mitochondria and melanosomes, we compared wild-type (melan-a) and albino (melan-c2) melanocytes, which lack melanin due to a loss-of-function mutation in the Tyr gene (Fig. S1A, B). These cells lack melanin synthesis, which in turn blocks melanosome maturation and causes an accumulation of early-stage melanosomes (stages I and II). Given the abnormal accumulation of immature melanosomes in albino cells compared to pigmented cells, we reasoned that mitochondria-early melanosome communication could also be altered. In line with this idea, our analysis confirmed that albino cells accumulate early-stage melanosomes (I/II) and are characterized by increased contact sites with mitochondria (Fig. 1A, B). We observed that, as they mature, melanosomes appear closer to mitochondria, with this proximity being significantly greater in albino cells at stage I than in pigmented cells. (Fig. 1C). In parallel we performed a differential expression analysis on the two cell lines using RNA-seq and found a significant upregulation of mitochondrial genes in albino cells compared to pigmented ones (Fig. 1D, E; Fig. S1F; Supplementary Data 1).

Then, we isolated mitochondria-melanosome-ER fractions (MMERF) from melan-a and melan-c2 cells and analyzed them by mass spectrometry (MS) (Fig. 1F, G and “Methods” section). To identify membrane-bound proteins involved in mitochondria-organelle interactions, we subjected MMERFs to limited proteolysis (Fig. 1F, G; Fig. S1G). Proteins identified in both treated and untreated fractions were considered luminal, being protected from the added proteases. To confirm which proteins were exposed on the surface of organelles, we exploited the topology of TYRP1. TYRP1 is a melanosome membrane protein with domains facing either the cytosol or the organelle lumen. We used two different antibodies, each of which could target one of the two regions with different exposure. This served as a control to ensure that proteinase K degraded only the exposed,

cytosolic parts of proteins (Fig 1L) . Proteins identified only in the untreated MMERF fractions were considered to be exposed to the organelle surfaces due to their susceptibility to proteolysis (Fig. 1F, G, L, and Fig. S1G). A Venn diagram of the proteomic datasets obtained from the two cell lines revealed 109 common proteins, with 136 enriched in melan-a and 242 in melan-c2 (Fig. 1H; Supplementary Data 2). Functional annotation showed that MMERFs from melan-a were enriched in Golgi and proteasome-related proteins, while MMERFs from melan-c2 contained more lysosomal, ER, and outer mitochondrial membrane (OMM) proteins (Fig. 1F). The list of OMM candidates included proteins previously retrieved at mitochondria-derived vesicles (MDVs), membrane contact sites (CTP1A, FUNDC2, MAVS, MTOR, RHOT2, TOM20, TOM34, TOM70)<sup>21</sup> and, unexpectedly, the mitochondrial fission factor MFF.

Although we could not observe morphological differences in the mitochondria network between healthy and pigmented melanocytes (Fig. S1J, K), we noticed that albino melanocytes were characterized not only by an accumulation of early melanosomes, but also by an increased size of the organelles (Fig. S1J-M). Therefore, we conducted a thorough examination to determine whether there were any changes in melanosome dynamics between the two cell lines (Fig. 1I). Using LysoTracker to monitor melanosome dynamics as done previously<sup>22,23</sup>, we observed that, despite having larger melanosomes, albino cells showed more fission events (Fig. 1I, J, K). Interestingly, fusion events in albino cells were also more frequent (Fig. S1O, P). These results suggested that the loss of function of TYR in albino cells leads to defective melanosome dynamics: in these cells, melanosome fusion rates would be outpaced by fission due to the inability to progress with melanin synthesis and with maturation of the organelles. Since MFF has been implicated in the division of different organelles, not only mitochondria, we hypothesized that it could participate in melanosome maturation.

## **MFF can bud from mitochondria to melanosomes and resides at melanosome constriction sites**

MFF serves as a membrane adaptor for the dynamin-like GTPase DRP1 in mitochondria and peroxisomal division<sup>24-26</sup>. Hence, MFF is also present in non-mitochondrial locations, where it facilitates membrane fission<sup>27</sup>. We investigated MFF localization using immunogold electron microscopy. MFF was present at the surface of melanosomes at every stage of maturation, independent of the presence of nearby mitochondria (Fig. 2A). To further confirm MFF localization, we used super-resolution microscopy in cells that have been labelled with HMB45, a monoclonal antibody that marks early melanosomes, recognizing an epitope of the protein GP100. Following synthesis, GP100 is subject to several proteolysis steps, resulting in its conversion into the HMB45-reactive low molecular weight form (~35 kDa)<sup>28</sup>. This form is known to associate with the fibrillar content of melanosomes: as melanin is produced and deposited on the fibrillar matrix, the HMB45-reactive epitopes gradually become covered, and by the time melanosomes mature into Stage III, reactivity with HMB45 is lost<sup>28</sup>. We found MFF-positive puncta at the surface of melanosomes both in melan-a and melan-c2 melanocytes (Fig. 2B, C, D, E). MFF puncta were not positive for TOMM20 or PDH, excluding the possibility of being part of mitochondria or MDVs (Fig. S2B). At steady state, approximately 22% of melanosomes marked by HMB45 were found to have MFF puncta in melan-a cells (Fig. 2F). Some MFF puncta colocalized with the mature melanosome marker TRP1, though to a lesser extent than with HMB45 (Fig. S2A). Quantitative analysis revealed that MFF and mtRFP colocalized less in albino melanocytes compared to pigmented melanocytes, suggesting a larger pool of non-mitochondrial MFF in albino cells (Fig. 2G). Consistent with this, we observed increased colocalization of MFF with HMB45 in albino melanocytes (Fig. S2C). Endogenous MFF was detected not only on the melanosome surface but also at membrane constriction sites and in vesicular/tubular extensions of

early melanosomes (Fig. 2H). Quantitative analysis indicated that MFF was associated with approximately 25% of the observed melanosomal fission regions (Fig. 2I), suggesting that there may be distinct fission sites as reported also for other organelles<sup>29</sup>. Therefore, we sought to understand whether MFF is directly involved in melanosome fission. First, we generated melan-a MELANO-IP cells, and then we verified the presence of MFF in pure melanosomal fractions, free of mitochondrial contamination (Fig. S2D, E). We found that isoform 1 of MFF was enriched in melanosomal fractions, whereas isoform 4 appeared more enriched in the total input (Fig. S2D, E). Overexpression of eGFP-MFF isoform 1 confirmed its localization at HMB45-positive structures and fission sites (Fig. S2F). To verify how MFF could be delivered to melanosomes, we performed time-lapse experiments by marking them with LAMP1-RFP, which had been previously found enriched in these organelles<sup>30</sup> and which co-localized with HMB45 in melan-a (Fig. 2B).

With this approach, we observed eGFP-MFF isoform 1 budding from mitochondria and moving toward LAMP1-RFP-positive structures (Fig. 2J). This result was also confirmed by staining stage I/II melanosomes, which have an acidic lumen, with LysoTracker (Fig. S2G). Of note, although we had evidence of MFF being trafficked from mitochondria to melanosomes, we cannot exclude the possibility that cytosolic pools of MFF exist, which may also be independently targeted to these organelles. Super-resolution time-lapse imaging highlighted the presence of MFF puncta at the neck of melanosome tubules, with membrane constriction and scission occurring at or near MFF puncta (Fig. 2K). Figure 2K shows that melanosome membranes can be split into two separate vesicular structures by an MFF punctum, with which they can remain attached (left example) or be released (Fig. 2K, right example). These results demonstrate that MFF associates with melanosomes and that it is enriched at fission sites independently of mitochondrial proximity, likely facilitating melanosome membrane fission.

## **MFF depletion disrupts melanosome fission and promotes lysosomal protease-mediated degradation**

Melanosomes have previously been shown to undergo vesicular and tubular fission, a mechanism critical for regulating their composition and function<sup>15</sup>. Thus, considering our results, we hypothesized that the recruitment of MFF to the melanosome surface may control their maturation by mediating fission events. Given that MFF is a known receptor for DRP1 (dynamin-related protein 1) - the GTPase responsible for mitochondrial membrane fission—we assessed if Drp1 could be involved in MFF-mediated melanosome fission. We investigated the potential colocalisation of DRP1 and MFF in melan-a cells. Using immunofluorescence, we detected DRP1 at the melanosome surface, similarly to MFF. However, minimal to no colocalization between the two proteins was observed at melanosomes (Fig. 3A). To further explore their eventual function in melanogenesis, we performed siRNA-mediated knockdown (KD) of both *Mff* and *Drp1* in wild-type melanocytes (Fig. 3B; Fig. S3A, B). Interestingly, knocking down either gene led to reduced expression of melanogenic proteins (Fig. S3C-E). However, while intracellular melanin levels were slightly reduced in *Drp1*-KD cells, they were significantly increased in *Mff*-KD cells (Fig. S3F). This increase in melanin could be explained by either enhanced melanin synthesis or the accumulation of dysfunctional, immature melanosomes. Given the reduced levels of melanogenic markers, we excluded the former and focused on the possibility of impaired melanosome maturation. Using SR microscopy, we observed that HMB45-positive melanosomes were enlarged only in *Mff*-silenced melan-a cells (Fig. 3C). The number of HMB45-positive melanosomes remained unchanged in both knockdown conditions (Fig. 3D), but the melanosomes were significantly larger only in *Mff*-silenced cells (Fig. 3E; Fig. S3H). TEM further confirmed that *Mff*-KD cells harbored larger melanosomes, often connected by narrow, neck-like structures, or

appearing as a fusion of melanosomes at different maturation stages (Fig. 3F; Fig. S3L, M). The presence of these hybrid early–late stage melanosomes suggests the inability to complete fission and that melanogenesis does not progress properly in the absence of MFF. Indeed, we observed a significantly lower frequency of fission events in *Mff*-KD cells compared to controls (Fig. 3G, H). Additionally, the colocalization of pigmented melanin granules (visible in brightfield) with HMB45-positive melanosomes was significantly higher in *Mff*-KD cells, further supporting the presence of hybrid melanosomal structures (Fig. 3I, J).

Interestingly, despite reduced fission frequency, melanosomal fission was not entirely abolished in *Mff*-silenced melanocytes. This is consistent with previous observations that MFF is not present at all visible melanosomal constriction sites (Fig. 2I), and it suggests that alternative fission mechanisms may exist.

To test whether MFF overexpression could influence melanosome morphology, we overexpressed all four MFF isoforms and assessed melanosome size (Fig. S3O). MFF overexpression alone was insufficient to promote melanosome fragmentation, supporting that MFF is not the sole mediator of melanosome division.

Defective melanosome membrane remodeling and fission result in increased melanosome size and accumulation of undegraded or unnecessary proteins, ultimately leading to impaired melanogenesis<sup>15,17</sup>. To better understand how MFF and DRP1 depletion differentially impact melanosome homeostasis, we performed RNA sequencing on *Mff*- and *Drp1*-silenced melanocytes. *Mff* silencing led to the upregulation of genes associated with the homeostasis of lysosomes (*Capn2*, *Ctsb*, *Ctsd*, *Dpp7*, *Gabarap*, *Kxd1*, *Lipa*, *Lrrc8a*, *Mfsd12*, *Mt1*, *Myo5a*, *Plekhm2*, *Rab7b*, *Scarb2*, *Siae*, *Sidt2*, *Tpcn1*, *Tpp1*), melanosomes (*Capg*, *Ctsb*, *Ctsd*, *Mfsd12*, *Myh11*, *Myo5a*, *Tpp1*, *Trpv2*, *Kxd1*) or both (*Ctsb*, *Ctsd*, *Mfsd12*) (Supplementary Data 3). These transcriptional changes were not observed in *Drp1*-silenced cells, which instead showed a broad

downregulation of key melanogenesis regulators, including Microphthalmia-associated transcription factor (MITF) (Fig. 4A; Supplementary Data 3). These findings confirm that *Mff* and *Drp1* silencing have distinct functional consequences in pigmented cells. While *Mff*-KD triggers the upregulation of lysosomal and catabolic genes, including cathepsins (*Ctsb*, *Ctsd*) and lysosomal lipase (*Lipa*), *Drp1*-KD primarily alters melanocyte differentiation and pigment production by downregulating transcriptional regulators such as MITF. As to the specific upregulation of lysosomal/catabolic genes in *Mff*-KD, we hypothesized that this response may reflect a compensatory mechanism triggered by impaired melanosome fission. Supporting this, CTSB protein levels were elevated in *Mff*-silenced melanocytes, which showed an increased colocalization of CTSB and HMB45-positive melanosomes (Fig. 4B–E). CTSB enzymatic activity was also significantly increased in *Mff*-KD cells (Fig. 4F, G). These data suggest that MF depletion promotes the trafficking and activity of lysosomal enzymes like CTSB, which are key in the process of melanosomes degradation<sup>31,32</sup>. Their enhanced melanosome localization could be potentially due to either increased melanosome–lysosome fusion or increased trafficking of lysosomal hydrolases, resulting in their partial conversion to a lysosome-like state. Both scenarios are consistent with a shift toward increased melanosome degradation, which is likely a compensatory response to blocked fission. To confirm this hypothesis, we assessed melanosomal acidification, a hallmark of lysosomal activity and of early melanosome, whose pH undergoes neutralization during maturation. Acidification was significantly increased in *Mff*-KD cells, but it was rescued to control levels by co-silencing CTSB (Fig. 4H, I). Notably, combined silencing of *Mff* and *Ctsb* restored the expression of melanogenesis markers (downregulated in *Mff*-KD alone) and further increased both melanin content and melanosome size, compared to *Mff* silencing alone (Fig. 4J, K, and Fig. S4C-I). Consequently, when CTSB-mediated melanosomal degradation was suppressed in *Mff*-KD cells, a marked accumulation of early-stage melanosomes was observed per

total cell area (Fig. 4L), which was not detected in *Mff* silencing alone (Fig. 3D). These findings indicate that the degradation of key melanogenic proteins (such as TYR, TRP1, and GP100) is enhanced in *Mff*-KD cells due to increased recruitment and activity of lysosomal enzymes within the melanosome lumen. This could represent a negative feedback mechanism aimed at reducing melanosome buildup when fission is impaired.

In summary, MFF depletion impairs early-stage melanosome maturation and triggers a compensatory upregulation of lysosomal catabolism to prevent the accumulation of dysfunctional or oversized melanosomes in response to decreased DRP1-independent melanosome fission.

### **MFF-dependent melanosome fission requires ARP2/3-mediated F-actin assembly**

Our data suggest that MFF can modulate the maturation of melanosomes by controlling their membrane fission independently of DRP1. To shed light on the molecular mechanisms of MFF-mediated melanosome fission, we determined the MFF interactome by immunoprecipitating it from melan-a whole cell lysate and identified the co-purified proteins by MS (Supplementary Data 3). The list of interacting proteins was enriched in actin cytoskeleton organization regulators, including subunits of the WASH core complex (Fig. 5A). This complex functions as an actin nucleation-promoting factor at the surface of endosomes and melanosomes, recruiting the ARP2/3 complex and allowing actin polymerization for vesicle/tubule fission<sup>15,33</sup>. FAM21C and Strumpellin (Kiaa0196) are key members of the WASH complex that appeared as hits from our IP (Fig. 5A). After confirming their interaction with MFF (Fig. 5B) and close apposition with early and late-stage melanosomes (Fig. S5G), we verified if their downregulation could affect early melanosome morphology (Fig. S5A, B, C). In melan-a cells, depletion of either of the two leads to no significant changes (Fig. S5D, E). These results suggest that the different components of the complex may have redundant functions and may compensate for each other. A gene ontology (GO) analysis of the MFF interactome also highlighted that the actin nucleation complex may be

involved in MFF function (Fig. 5C). Therefore, to clarify the contribution of actin filaments to MFF-mediated melanosome fission, we co-stained melan-a expressing eGFP-MFF with phalloidin and HMB45 (Fig. 5D). We observed F-actin at and in between MFF-positive melanosome constriction sites (Fig. 5D,E). Because ARP2/3 complex-mediated actin nucleation was among the enriched GO terms (Fig. 5C), we sought to understand whether the effect of MFF depends on the ARP2/3 complex by silencing two different subunits: ARPC1A and ARPC3 (Fig. S5H-J). Their silencing led to increased early melanosome size, which was more noticeable when ARPC1A was silenced (Fig. 5F). ARPC1A silencing also led to a change in intracellular melanin levels (Fig. S5K). Besides, we confirmed ARP2/3 complex subunit localization at MFF-HMB45-positive melanosomes (Fig. 5G), and we found that MFF puncta locate in proximity to the enlarged melanosomes in ARPC1A/ARPC3-silenced cells (Fig. S5L). This evidence suggests that the recruitment of MFF to melanosomes is independent of the ARP2/3 complex. Silencing of MFF led to increased melanosome size, consistent with a role in promoting organelle fission. However, co-treatment with the Arp2/3 inhibitor CK-666 (a small molecule that stabilizes the ARP2/3 complex in its inactive state and thereby blocks actin nucleation) abrogated this phenotype, suggesting that melanosome enlargement in the absence of MFF requires active actin polymerization (Fig. 5H).

## DISCUSSION

Here we identified MFF as part of the fission machinery of melanosomes. While MFF was found in fission sites of mitochondria and peroxisomes, its role in melanosomes was not described before<sup>24,25</sup>. We found that MFF recruits ARP2/3-interacting proteins at the surface of melanosomes, to

facilitate membrane constriction and fission through F-actin nucleation-associated factors. This process is crucial for maintaining the shape and identity of melanosomes during the early stages of maturation. Indeed, MFF ablation leads to an increase in the size of early melanosomes and to the acquisition of lysosome-like catabolic features, likely due to elevated demands for luminal protein degradation resulting from impaired membrane scission. Importantly, MFF-mediated fission does not require its classical partner DRP1: they do not colocalize and, surprisingly, the effects of their downregulation in melanocyte physiology were proven different. Our data show that the MFF-mediated melanosomes fission is needed for the release and export of components that are either required in other melanosomes or that should not be retained for the proper maturation of melanosomes, as previously suggested<sup>15</sup>.

It was described that mitochondria and mitochondrial proteins can play important roles in melanosome maturation, pigmentation, and transport, through direct localization to melanosomes or by mediating communication between the two organelles<sup>18,19,34</sup>. Moreover, early-stage melanosomes are known to closely associate with mitochondria, likely supporting melanogenesis<sup>19</sup>. Comparing pigmented (melan-a) and albino (melan-c2) melanocytes, which harbour a mutated form of TYR that inhibits melanin synthesis and hence melanosome maturation, we observed an accumulation of immature melanosomes and an increase in mitochondria-melanosome contact sites in albino cells. Transcriptomic and proteomic analyses highlighted an enrichment of OMM proteins in albino cells, including MFF. Surprisingly, while mitochondrial morphology remained unchanged, albino cells showed elevated rates of melanosome fission and fusion, indicating disrupted organelle dynamics. Using different approaches, we detected MFF at the membranes of melanosomes across all maturation stages, independent of mitochondrial proximity. Super-resolution microscopy confirmed MFF colocalization with early melanosomes marked by HMB45, and to a lesser extent with mature melanosomes marked by TRP1. MFF puncta

did not overlap with TOM20 or PDH, ruling out the possibility of being mitochondrial or MDVs. Notably, albino cells displayed increased MFF-HMB45 colocalization and reduced MFF-mitochondria association, supporting a larger pool of non-mitochondrial MFF is present in response to TYR loss. Further, we could observe that MFF localized to constriction sites and tubulovesicular extensions of early melanosomes, with ~25% of melanosomal fission regions being associated with MFF. This suggests that different fission mechanisms may exist, likely being responsible for the scission of different melanosomes or different subdomains of melanosomal membranes, probably depending on their composition, localization, or specific cell requirements. This would be in line with the heterogeneity that characterizes fission of other organelles, like mitochondria, for which it was shown that different protein adaptors mediate distinct types of fission, linked either to degradation or organelle biogenesis<sup>29</sup>.

Isoform-specific analyses revealed that MFF isoform 1 is enriched in purified melanosomal fractions and localizes at melanosome fission sites. Live-cell imaging showed MFF that redistributes from the mitochondria towards LAMP1-RFP-positive compartments and LysoTracker-labelled acidic structures. However, since MFF also exists in cytosolic pools, it may also be trafficked independently to melanosomes. Moreover, our results identify an unexpected role for the mitochondrial fission factor MFF in melanosome morphology and maturation. In mitochondria, MFF acts in concert with DRP1 which made us investigate whether this was the case for melanosomes<sup>10,35,36</sup>. Although both MFF and DRP1 were observed at melanosome surfaces, they rarely colocalized. siRNA-mediated knockdowns of MFF and DRP1 in wild-type melanocytes yielded different effects: while DRP1 depletion slightly reduced melanin levels and downregulated melanogenesis genes like MITF, MFF depletion led to enlarged early-stage melanosomes, with reduced fission events and increased colocalization with melanin. Thus, DRP1 depletion primarily affects transcriptional regulation of melanosome biogenesis, whereas MFF

depletion impairs progression of melanosome maturation. RNA-seq of *Mff*-silenced cells showed upregulation of lysosomal and melanosomal catabolic genes (e.g., *Ctsb*, *Ctsd*, *Lipa*), a transcriptional response not observed in *Drp1*-KD cells. This result was confirmed by higher CTSB protein levels and activity within melanosomes and enhanced acidification, indicating a shift toward melanosome degradation/lysosomal-like phenotypes. Supporting this idea, co-silencing of *Ctsb* with *Mff* restored the elevated melanosomal acidification and the expression of melanogenesis markers, increased both melanin content and melanosome size, and led to a marked accumulation of immature melanosomes. These findings indicate that MFF regulates melanosome fission independently of DRP1, and that its loss triggers a compensatory pathway to degrade dysfunctional melanosomes and preserve cellular homeostasis. Mass spectrometry of the MFF interactome in melanocytes revealed enrichment of actin cytoskeleton regulators, including components of the WASH complex, known to promote ARP2/3-mediated actin nucleation<sup>15,37</sup>. Knockdown of individual WASH components did not alter melanosome size, likely due to redundancy. However, F-actin was found to accumulate at MFF-positive melanosome constriction sites, and two key components of the ARP2/3 complex subunits (e.g., ARPC1A, ARPC3) colocalized with MFF at melanosome membranes. Silencing of *Arpc1A* and *Arpc3* led to the appearance of enlarged early melanosomes. Notably, MFF remained at melanosomes even in these conditions, indicating an upstream recruitment of MFF to melanosomes that is independent of ARPC2/3 activity. Overall, our findings confirm that MFF facilitates melanosome fission by recruiting the ARP2/3 actin-nucleation machinery. Several human disorders, including Chédiak-Higashi syndrome<sup>38</sup>, X-linked ocular albinism<sup>39</sup>, and Ocular albinism type I<sup>40</sup>, are characterized by the presence of giant melanosomes, also known as macromelanosomes. Despite the genetic causes of these diseases being known, the exact mechanism leading to the formation and accumulation of abnormal melanosomes is still unclear, although defective biogenesis and

maturation of the organelles have been proposed<sup>40</sup>. Our findings may be relevant not only to advancing the understanding of pigmentary disorders and the etiology of pigmented and amelanotic melanoma, but also to identifying MFF as a potential drug target. Given its role in melanosome maturation, further investigation of MFF may offer insights into both conditions and highlight the involvement of mitochondrial proteins in melanosome physiology<sup>41</sup>.

## **METHODS**

### **Cell culture: melan-a and melan-c2**

Melan-a melanocytes are normal, immortalized murine melanocyte cells derived from C57BL/6J mice. Melan-a melanocytes were obtained from the Functional Genomics Cell Bank at St. George's University of London, UK<sup>42</sup>. Melan-a melanocytes were maintained in a RPMI-1640 medium (Euro Clone, Cat. No. ECB2000L; Supplementary Table 1) supplemented with 10% fetal bovine serum (FBS) (Euro Clone, Cat. No. ECS0165L), 100 U/mL penicillin, 100 µg/mL streptomycin, and 200 nM phorbol 12-myristate 13-acetate (PMA; Sigma-Aldrich, Cat. No. P8139). PMA was diluted in phosphate-buffered saline (PBS) containing 1% FBS to obtain a 40 µM stock solution. Melan-c2 melanocytes are immortalized tyrosinase mutant murine melanocytes (Tyrc-2J/Tyrc-2J, a functionally null allele) derived from C57BL/6J. Cells were maintained in RPMI-1640 medium supplemented with 10% FBS, 100 U/mL penicillin, 100 µg/mL streptomycin,

and 200 nM PMA and 2 nM cholera toxin diluted in water (Sigma-Aldrich, St. Louis, MO, Cat. No. C8052). Both cell lines were kept at 70% confluency between experiments at 37°C in a 10% CO<sub>2</sub> incubator.

### **Virus production and generation of melan-a stably expressing HA-MelanoTag and Myc-MelanoTag**

Lentiviruses were produced by co-transfection of HEK 293T cells with a target lentiviral transfer vector (2,5 µg HA-MelanoTag (Addgene #160369) and Myc-MelanoTag (Addgene #160368)), pMD2.G (0,5 µg, Addgene #12259), and psPAX2 (2 µg, Addgene #12260) plasmids. Virus-containing supernatants were collected 48 h post-transfection, and transduction was performed. About 2,0x10<sup>6</sup> melan-a cells were incubated for infection with 5 mL of viral supernatant, 8 µg/ml polybrene, and 5 mL culture medium in a T75 flask. Infected cells were passaged into medium containing puromycin (3 µg/ml) 36–48 h post-transduction. Selection was maintained for 7 days before use of the cells.

### **Intracellular melanin content assay**

1 x 10<sup>6</sup> cells were plated on a 100 mm cell culture Petri dish. After 66 h, cells were scraped in PBS and lysed using RIPA buffer (50 mM TRIS pH 8, 1% NP-40, 0.5% Na-deoxycholate, 0.1% SDS, 150 mM NaCl, 2 mM EDTA) supplemented with protease (Thermo Fisher Scientific, Cat. No. A32955) and phosphatase (Thermo Fisher Scientific, Cat. No. A32957) inhibitors for 30 min, on ice. After centrifugation at 16,500 x g for 15 min at 4°C, the supernatant was collected for protein assay, and the melanin pellet was solubilized in 1 N NaOH with 10% DMSO for 90 min at 80°C. Then, sample absorbance was acquired at 450 nm and the values were compared with a standard

curve of synthetic melanin (Sigma-Aldrich, #M8631). Samples were normalized for total protein content (Bradford method, Bio-Rad, Cat. No. 5000006).

### **Mitochondria-Melanosome-ER- fraction (MMERF) isolation**

Cells were plated at 80% confluency in a Corning® square dish (245x245 mm; CLS431110-16EA Corning). After 24 h, they were harvested and washed once with cold PBS. The cell pellet was then resuspended in 700 µl of mitochondrial isolation buffer (containing 200 mM mannitol, 70 mM sucrose, 1 mM EGTA, 10 mM HEPES; 1X protease inhibitor cocktail (Thermo Scientific, Cat. No. A32955)). Homogenization was performed on ice using a 1 ml insulin syringe. Cells were centrifuged at 1,000 x g for 10 min at 4°C, and the supernatant was collected while the pellet, corresponding to the PNS fraction, was retained for further processing. The supernatant was spun at 12,500 x g for 15 min at 4°C. After centrifugation, the new supernatant (enriched with cytosolic and microsome components) and a part of the pellet (corresponding to crude mitochondria) were stored for Western Blot analyses. Crude mitochondria were washed with 1 ml isolation buffer and centrifuged again at 12,500 x g for 10 min, thereby obtaining MMERF. The pellet was resuspended in 60 µl of mitochondrial isolation buffer and protein concentration was determined using Bio-Rad Protein Assay Reagent (Bio-Rad, Cat. No. 500000). MMERF were treated on ice for 15 min with proteinase K (Invitrogen, Cat. No. AM2548) in a final concentration of 15 µg/ml diluted in mitochondrial isolation buffer. Proteinase K was subsequently blocked with 5 mM phenylmethylsulfonyl fluoride (PMSF, Sigma-Aldrich Cat. No. 78830) for 5 min on ice. 20 µg of each sample (either proteinase K-treated or not) was loaded for western blotting; 70 µg were used for the MS analysis, and 15 µg of MMERF were fixed for TEM.

### **Mass spectrometry sample preparation**

Proteins were precipitated and concentrated by adding 4 volumes of ice-cold MS-grade Acetone (over-night incubation) and pelleted at 20,000 xg for 20 min, at 4°C. The protein pellet was additionally washed with ice-cold 70% ethanol. Then a standardized in solution digestion protocol was applied. Briefly, dried proteins were dissolved in 6M guanidine hydrochloride (GnHCl), 50 mM Tris pH=8.5, reduced by incubation with 10 mM Tris-(2-carboxyethyl)phosphine-hydrochloride (TCEP) and alkylated with 40 mM chloroacetamide (CAA). Then, they were digested overnight (37°C) adding a mix of Lys-C/Trypsin hydrolases in a 1:50 enzyme to protein ratio. The hydrolysis reaction was quenched by adding 1% trifluoroacetic acid (TFA). The resulting peptide mixtures were desalted using the Stop and Go Extraction (STAGE) procedure and then lyophilized and stored at -20°C until the MS analysis (PMID: 12585499). All the experiments were performed in triplicate starting from three different immuno-precipitations. As controls, we performed, in triplicate, immuno-precipitations without the specific antibody against our target.

### **Mass Spectrometry Analysis**

Instruments for LC-MS/MS analysis consisted of a NanoLC 1200 (Thermo Fisher Scientific) coupled via a nano-electrospray ionization source to the quadrupole-based Q Exactive HF (ThermoFisher Scientific) benchtop mass spectrometer<sup>43</sup>. Peptide separation was carried out according to their hydrophobicity on a home-made column, 75 µm ID, 8 µm tip, 250 mm bed packed with Reprosil-PUR, C18-AQ, 1.9 µm particle size, 120 Å pore size (New Objective, Inc., Cat. No. PF7508-250H363), using a binary buffer system consisting of solution A: 0.1% formic acid and B: 80% acetonitrile, 0.1% formic acid. Total flow rate: 300 nl/min; LC linear gradient: after sample loading, the run starts at 5% buffer B for 5 min, followed by a series of linear

gradients, from 5% to 30% B in 90 min, then a 10 min step to reach 50% and a 5 min step to reach 95%. This last step was maintained for 10 min. MS spectra were acquired using 3E6 as an AGC target, a maximal injection time of 20 ms, and a 120,000 resolution at 200 m/z. The mass spectrometer operated in a data-dependent Top20 mode with subsequent acquisition of higher-energy collisional dissociation (HCD) fragmentation MS/MS spectra of the top 20 most intense peaks. Resolution for MS/MS spectra was set to 15,000 at 200 m/z, AGC target to 1E5, max injection time to 20 ms, and the isolation window to 1.6 Th. The intensity threshold was set at 2.0E4 and Dynamic exclusion at 30 s.

### **Mass spectrometry Data Processing**

MaxQuant software (1.6.2.10) was used for protein identification and label-free quantification. Trypsin (Thermo Fisher Scientific) was chosen as the enzyme and the number of missed cleavages was set to 1. Cysteine carbamido-methylation was set as a fixed modification, whilst methionine oxidation and N-term acetylation were used as variable modifications. Uniprot Mus Musculus (UP000000589) FASTA file was used as database (accessed in 2023). The maximum false discovery rate (FDR) for peptide spectral match was set to 1%, using a minimum of one sequence-unique peptides was required for identification. Statistical analyses for quantitative evaluation were performed using the open-source Perseus software (1.6.2.3). Two-sample t-test analysis was applied, setting the level of significance equal to 0.05. Proteins with at least one-fold changes were considered differentially regulated. Proteins of interest were further investigated for GO enrichment terms with ShinyGo platform. The mass spectrometry proteomics data have been deposited to the ProteomeXchange Consortium via the PRIDE partner repository<sup>44</sup> with the dataset identifier PXD051372.

### **Library preparation and mRNA sequencing**

Melan-a and melan-c2 cells underwent lysis and RNA extraction using Trizol® (Thermo Scientific Cat. No. 15596018) according to the manufacturer's protocol. The purity and concentration of samples were checked with a NanoDrop spectrophotometer (ND 1000, Thermo Fisher Scientific). The libraries were generated with the QuantSeq 3' mRNA-seq Library Prep kit (Lexogen) and oligodT priming. After the first strand synthesis, the RNA was removed. A second strand synthesis was initiated using random priming followed by magnetic bead-based purification. The libraries were then amplified, introducing the sequences required for cluster generation. External barcodes were introduced during the PCR amplification step. Library quantification and quality control were performed using a fluorometer (Qubit, Thermo Fisher scientific) and Bioanalyzer 2100 (Agilent). NGS reads were generated towards the poly(A) tail. Sequencing was performed on NextSeq500 Illumina instrument to produce at least  $5 \times 10^6$  reads (75 bp SE) for each sample.

### **Analysis of RNA-Seq data**

Quality of sequencing reads was evaluated with fastqc v0.11.9, plus multiqc v1.6<sup>45</sup>, then the reads were trimmed with fastp v0.20.1<sup>46</sup> by removing 15 nt at 5', 2 nt at 3', discarding all those reads containing "N" characters, removing heading and trailing homopolymers, removing heading and trailing low-quality portions and retaining only trimmed reads with length of at least 35 nt. All the other settings for the trimming were left as default. Trimmed reads were mapped on the cDNA sequences from the reference mouse genome (GRCm39) with salmon v1.8<sup>47</sup> with the validate Mappings flag and by providing the transcript to gene map in order to obtain gene-level expression measurements in terms of counts. A first check of coherence between samples was performed by visual inspection of Principal Component Analysis (PCA) and Multi-Dimensional Scaling (MDS) plots. Differential gene expression analysis was carried out with the edgeR package<sup>48</sup>: briefly genes with low counts were discarded (filterByExpr function), then expression values were

normalized, and a Generalized Linear Model (GLM) was fitted on the data. Differential expression between all possible pairs of samples was assessed using a quasi likelihood F-test for generalized linear models as implemented in edgeR, and p-values were adjusted for multiple testing using the Benjamini–Hochberg false discovery rate (FDR) correction. Genes with an FDR-adjusted p-value  $< 0.05$  (two-sided test) were considered differentially expressed. Gene Set Enrichment Analysis (GSEA) was performed on the Gene Ontology (GO) and annotations<sup>49</sup>. Specifically, a hypergeometric test was applied to the DEGs sets (also splitting up- and down-regulated DEGs)<sup>50</sup> using only expressed genes as “universe” (i. e. those obtained from the FilterByExpr function) to avoid biases<sup>51</sup>. Only GO terms supported by an FDR-corrected p-value  $< 0.05$  were considered as significantly enriched. Data visualizations were produced with seaborn and plotly.

### **Immunoblotting**

Melanocytes were lysed with ice-cold RIPA buffer supplemented with protease inhibitor cocktails (Thermo Fisher Scientific, Cat. No. A32955). Cell lysates were then centrifuged at  $16,500 \times g$  for 15 min at  $4^{\circ}\text{C}$  and the supernatant protein content was determined using the Bradford reagent (Bio-Rad, Cat. No. 5000006). After heating at  $70^{\circ}\text{C}$  for 10 min, equal amounts of protein ( $30 \mu\text{g}$ ) were loaded onto precast gels (ExpressPlus™ PAGE Gel, Genscript 4-12% or 4-20%) and separated electrophoretically in Tris-MOPS running buffer (Genscript, Cat. No. M00138). After electrophoresis, the proteins were blotted onto a polyvinylidene fluoride membrane (PVDF) (EMD Millipore, Merck, Cat. No. IPVH85R). The blocking was performed for 1 h at RT using 5% milk (Sigma Aldrich, Cat. No. 70166) in Tris-buffered saline with 0.1% Tween 20 (TBS-T), and the membrane was incubated with the selected primary antibodies O/N at  $4^{\circ}\text{C}$  (listed in Supplementary Table 2). After washing, the membranes were incubated with HRP-conjugated anti-Rabbit secondary antibody (1:4000; Cell Signalling, Cat. No. 7074-P2) and HRP-conjugated anti-Mouse

secondary antibody (1:2000/1:4000, Cell Signalling, Cat. No. 7076-P2) for 1 h at RT. Secondary antibodies details are provided in Supplementary Table 3. The signal was visualized using an enhanced chemiluminescence kit (Luminata Forte Western HRP (Millipore Sigma WBLUF0500) according to the manufacturer's instructions and acquired using iBright™ CL1500 (Invitrogen), ImageQuant LAS 4000 Mini (GE Healthcare), or the ChemiDoc MP Imaging System (BioRad). For two-color fluorescence imaging of membranes Odyssey CLx Imager from LI-COR Biosciences was used.

### **Melanosome immunoprecipitation (Melano-IP)**

Melan-a cells ( $3 \times 10^6$ ) expressing MelanoTag were plated into a 15-cm plate. Two days later, cells were collected for Melano-IP. Cells were washed and collected by scraping in ice-cold KPBS (136 mM KCl, 10 mM KH<sub>2</sub>PO<sub>4</sub>, pH 7.25 adjusted with KOH)<sup>30</sup> before pelleting by centrifugation at 1000g for 2 min at 4 °C. Pellets were resuspended in 950 µl ice-cold KPBS, and 50 µl of the cell suspension was taken as a whole-cell fraction (Input). Homogenization was performed on ice using a 1 ml insulin syringe, and then samples were centrifugated at 1000g for 2 min at 4 °C. Supernatants were transferred into new 1.5-ml tubes containing 100 µl of KBPS-washed Pierce™ Anti-HA Magnetic Beads (Thermo Fisher) and incubated rocking for 15 min at 4 °C. Beads were washed 3 times with 1 mL ice-cold KPBS, transferring to a new 1.5-ml tube each time. Whole-cell and immunoprecipitated samples were then lysed in 50 µl ice-cold RIPA buffer supplemented with protease inhibitor cocktails (Thermo Fisher Scientific, Cat. No. A32955).

### **MFF Immunoprecipitation**

Protein A beads (protein A - Agarose, Roche, Cat. No. 11719408001) were prepared in PBS with 0.1% BSA, and left to rotate at 4°C for 30 min. They were washed three times with 400 µl of PBS

and centrifuged at 200 x g for 1 min. Then, beads were resuspended in lysis buffer (50 mM Tris-HCl pH 7,5, 150 mM NaCl, 1 mM EGTA pH 7,5, 1 mM EDTA pH 7,5, and 1% Triton X-100) supplemented with protease inhibitor, and incubated with 3 µg of each antibody on a rotator at 4°C O/N. Protein A beads were washed with lysis buffer and centrifuged three times at 200 x g for 1 min. Whole cell lysates were prepared by collecting cells in cold PBS and resuspension in lysis buffer. The cell lysate was kept on ice for 10 min, sonicated (four times 5 pulses of 0.5 s), and then centrifuged at 14,000 x g for 15 min. The resulting supernatant was quantified with Bradford protein content. 2 mg of proteins were incubated with the bead-antibody conjugate O/N at 4°C. The next day, the beads-antibody-whole lysate complexes were spun five times at 200 x g for 30 s to remove the supernatant and add clean, fresh lysis buffer (300 µl each time). IP elution was performed by resuspension of the last in 50 µl of 2x Laemmli buffer containing 200 mM β-mercaptoethanol (Merck, Cat. No. M3148) with further denaturation for 5 min at 95°C.

### **Cloning and plasmids**

We generated eGFP-MFF plasmids (pEGFP-FlagMff-iso1, 2, 3, 4) starting from melan-a cells. RNA from melan-a cells was extracted using RNeasy Mini Kit (Qiagen, Cat. No. 74104) following the manufacturer's instructions. RNA was reverse transcribed in cDNA using GoScript Reverse Transcriptase (Promega, Cat. No. A5003). For Mff amplification, PCR was performed using melan-a cDNA, PrimeSTAR GXL DNA Polymerase (Takara technologies, Cat. No. R050A), and the primers specified in Supplementary Table 4. The amplicons were run in a 2% agarose gel to distinguish the different Mff isoforms according to their nucleotide sizes. The band corresponding to Mff isoform 2 appearing at ~720 bp was gel purified using Qiagen Gel Extraction Kit (Qiagen, Cat. No. 28704). The amplicon of Mff isoform2 and the vector pEGFP-C1 (Addgene, Cat. No. 6084-1) were digested with HindIII-HF (New England Biolabs NEB Cat. No. R3104S) and

BamHI-HF (New England Biolabs NEB Cat. No. R3136S) restriction enzymes, run in a 2% agarose gel and gel purified. The insert was ligated to the vector using T4 DNA Ligase (New England Biolabs NEB Cat. No. M0202S) following the manufacturer's instructions using a 3:1 ratio. The insertion was verified by Sanger sequencing.

### **Electroporation into melan-a and melan-c2 of siRNA and plasmids**

Microporation was done using either Neon™ Transfection System (Invitrogen, Cat. No. MPK5000) or Lonza® Nucleofector® electroporation system. Melan-a and melan-c2 at 80% confluency were detached with trypsin, counted, and centrifuged in serum-containing medium at 500 x g for 5 min. The cell pellet was resuspended in warm (37°C) PBS. Then,  $1,2 \times 10^5$  cells were electroporated with siRNA and/or plasmid DNA according to the manufacturer's instructions (10 µl volume, 40 nM final concentration of a pool of 4 siRNAs; sigenome SMART pool, Horizon Discovery 1 µg/ul for plasmids; Supplementary Data 4). After microporation (1,200 V, 20 ms, 3 pulses), cells were immediately resuspended with media (RPMI-1640 medium supplemented with 10% FBS) and 200 nM PMA, without antibiotics) and plated. 66 h after electroporation, cells were either fixed or collected for further analysis.

### **Melan-a cell lentiviral transduction**

For virak transduction, 10000 melan-a cells per well were seeded in 96-well plates, and cultured for 24 h at 37 °C in a humidified incubator with 10% CO<sub>2</sub>. Cells were then transduced with lentiviral particles encoding either shRNA targeting Mff or the non-targeting control (MISSION® pLKO.1-puro Non-Target shRNA Control Transduction Particles; Sigma-Aldrich, SHC016V). For Mff silencing, individual shRNA constructs were employed: TRCN0000174665 (target sequence: GATCGTGGTTACAGGAAATAA) and TRCN0000174539 (target sequence:

CTTCATTAAGACGTCAGATA; Sigma-Aldrich, MISSION® shRNA library). Transduction was performed in complete growth medium supplemented with 10 µg/mL polybrene (Sigma-Aldrich, #TR-1003) for 24 h at 37 °C in a humidified incubator with 5% CO<sub>2</sub>. Following transduction, cells were cultured in fresh complete growth medium for additional 24 h prior to downstream analyses.

### **HTS acquisition and analysis of mitochondria and melanosome morphology**

Melan-a/c2 cells were seeded on a 96-well TC-Treated Black µCLEAR microplate (Greiner Bio-One, Cat. No. 655090) and incubated in growth media for 48 h. Melanocytes were fixed with PBS containing 3.7% formaldehyde (Sigma-Aldrich, Cat. No. 252549) for 15 min, permeabilized with 0.1% Triton X-100 (Sigma-Aldrich, Cat. No. T8787) for 15 min and blocked with 5% BSA (Carlo Erba Reagents, Cat. No. A268131000) diluted in PBS for 1 h at RT. Cells were stained with the primary antibodies anti-TOM20 (diluted 1:150, Sigma-Aldrich, Cat. No. HPA011562) and HMB45, which is already diluted and ready-to-use (Agilent Technologies, Cat. No. GA052) O/N at 4°C. The cells were then washed three times with 5% BSA in PBS and incubated with the following secondary antibodies: Goat anti-Rabbit IgG (H+L) Alexa fluor 488 Secondary Antibody diluted 1:250 (Invitrogen Thermo Fisher Scientific, Cat. No. A-11070), Goat anti-Mouse IgG (H+L) Alexa Fluor 568 diluted 1:250 (Thermo Fisher Scientific, Cat. No. A-11004). Nuclei were stained with Hoechst 33342 200 µg/mL in PBS (Thermo Fisher Scientific, Cat. No. H1399) for 10 min at RT. Cells were later incubated with phalloidin 680 (Abcam, Cat. No. ab176760, diluted 1:500 in 1% BSA in PBS) for 90 min at RT for total cell area detection. After incubation, melanocytes were washed 3 times with PBS. Images were acquired using the Operetta CLS™ High-Content Analysis System (PerkinElmer), with a 63× Water/1.15 NA objective (High Content Imaging was performed at the HiTS@uniPD Facility, Department of Biology, Padua). Alexa Fluor

488/568, Hoechst, and phalloidin images were captured using 8 Z-stack planes at 1-micron step size using 460–490 and 355–385 nm excitation LEDs and emission filters 500-550 and 570-650, respectively.

Automated image analysis was performed with the Harmony® Analysis Software (PerkinElmer); a proprietary supervised machine learning algorithm (PhenoLOGIC™, Harmony® Analysis Software, Perkin Elmer) was used to quantify single-cell mitochondria and melanosome number and intensity, in addition to their mean area (px<sup>2</sup>), perimeter (px), and length (px). Z-stacks were processed to obtain maximum projections; nuclei segmentation based on Hoechst was followed by identification of the cytoplasm and HMB45/Tom20 positive particles.

### **Immunofluorescence and imaging**

Immunofluorescence was performed as previously described<sup>52</sup>. Cells were fixed with PBS containing 3.7% formaldehyde (Sigma-Aldrich, Cat. No. 252549) for 15 min, permeabilized with 0.1% Triton X-100 (Sigma-Aldrich, Cat. No. T8787) for 15 min and blocked with 5% BSA in PBS for 1 h, and then incubated O/N with primary antibodies diluted in PBS with 5% BSA at 4°C. After three washes with 5% BSA in PBS, cells were incubated with appropriate secondary antibodies prepared in 5% BSA in PBS solution for 1h at RT. Samples were rinsed three times with PBS and incubated with Hoechst 33342 (200 µg/mL for 10 min, diluted in PBS). After three additional washes with PBS, coverslips were briefly rinsed in MilliQ water and mounted onto glass slides using Mowiol. Cells were imaged using either an Axio Imager M2 laser scanning microscopy (LSM) 900 microscope (Carl Zeiss), equipped with an Airyscan module and a Plan-Apochromat 63x/1.40 Oil DIC M27 objective, or for super-resolution imaging, an Elyra 7 SIM<sup>2</sup> (Carl Zeiss Microscopy) equipped with a Plan-APOCHROMAT 63x/1.4 Oil DIC M27 objective. Images were acquired depending on the needs with the lasers (405, 488, 561, and 640 nm) and dichroic

filters QBS 405, 493,575, 653 and TBS 405, 493, 610 (16 bit) either in confocal or Airyscan mode (these were deconvoluted with standard Airyscan processing). SIM acquisition utilized all available fluorophores with appropriate laser lines and filters (filters: BP 495-550 + LP 655, BP 420-480 +BP 570-640 + LP 740, BP 495-550 + LP 655; camera exposure time of 50 ms; 13 phases, 16-bit). Z-stacks were acquired to ensure full volumetric coverage of the cellular structures, with optimal slice intervals for processing. Post-acquisition, raw SIM datasets were processed using the integrated ZEISS ZEN Black software with the SIM<sup>2</sup> algorithm to reconstruct super-resolved images (3D, leap). Quantification of MFF puncta and their colocalization with melanosome constriction points was performed on fixed melan-a cells stained for MFF and HMB45. MFF puncta and their overlap with fission zones were manually counted within two to three regions of interest (ROIs) per cell, each measuring 40  $\mu\text{m}^2$ .

### **Live imaging and quantification of melanosome fission and fusion**

Live imaging was performed on melan-a cells previously transfected with the eGFP-MFF (isoform 1) plasmid and LAMP1-RFP, cultured on an ibidi  $\mu$ -Slide 8 Well chambers (Cat. No. 80826). For LysoTracker-based imaging, cells were transfected with eGFP-MFF only when required. On the day of imaging, cells were incubated with 100 nM LysoTracker Deep Red (Molecular Probes, Thermo Fisher Scientific, Cat. No. L12492) and with 50 nM of MitoTracker<sup>TM</sup> Green FM (Molecular Probes, Thermo Fisher Scientific, Cat. No. M7514) in complete medium for 45 minutes. After incubation, the medium was replaced with fresh complete medium for microscopy. Live-cell super-resolution imaging was performed using a Zeiss Elyra 7 system equipped with Lattice SIM<sup>2</sup> (Carl Zeiss Microscopy) using a 13-phase acquisition protocol across all channels. Time-lapse videos were acquired over 30 cycles under physiological conditions (37 °C, 5% CO<sub>2</sub>). Image reconstruction was carried out in ZEN Black (Carl Zeiss Microscopy) using the SIM<sup>2</sup>

algorithm in two-step burst mode (2D Leap), yielding an approximate lateral (x, y) resolution of ~31 nm after deconvolution. Melanosome fission and fusion events were tracked using the TrackMate plugin in Fiji. Analyses were conducted either on defined regions of interest (ROIs) comparing melan-a and melan-c2 cells, or across full-cell areas following HUANG thresholding, using cells labeled with LysoTracker Deep Red or electroporated with LAMP1-RFP. To minimize artifacts from focal plane shifts, the number of fission (splitting) events was subtracted from the number of fusion (merging) events per spot detection. Spot area and perimeter measurements were extracted from the same plugin, considering only LysoTracker-labeled structures with a detected area exceeding  $0.5 \mu\text{m}^2$ .

### **Colocalization analysis**

For colocalization analysis of MFF, HMB45, and mito-RFP in melan-a and melan-c2 cells, Z-stacks were acquired with a step size of  $0.15 \mu\text{m}$ . Mito-RFP positive cells were processed using standard Airyscan super-resolution settings, and standard size ROIs ( $11.5 \mu\text{m} \times 11 \mu\text{m} = 126.5 \mu\text{m}^2$ ) were drawn in the cell cytosol. At least three per cell were analyzed. Maximum z-projections of all acquired stacks were generated for the three channels in the analyzed ROIs. On these ROIs, the Manders overlap coefficient was quantified using the JACoP plugin in the Fiji program<sup>53,54</sup>. The same analysis and ROI size were used for colocalization analysis of MFF, HMB45, and mito-RFP in CTSB silencing conditions (Table 3). The same procedure was used for colocalization analysis of HMB45 and CTSB in siRNA control/MFF conditions, but in total cell area ROIs. HMB45 colocalization with melanin was quantified from single-plane confocal images of the respective conditions, considering five cells per condition (two ROIs per cell,  $10 \mu\text{m} \times 10 \mu\text{m} = 200 \mu\text{m}^2$ ). Single plane images were selected for analysis based on the focal plane that allowed the maximum number of melanin BF spots to be identified.

**Magic Red® (Cathepsin B assay) and acridine orange (AO)**

Melan-a cells were seeded on a 96-well Ultra microplate (PerkinElmer) after electroporation with the appropriate siRNA conditions and incubated in growth media for 66 h. Melanocytes were incubated for 1 h at 37°C and 10% CO<sub>2</sub> with Magic Red reagent (Cathepsin B Assay Kit - Magic Red® Abcam, Cat. No. AB270772) diluted in DMSO according to the manufacturer's instructions. For AO staining (Sigma Aldrich, Cat. No. 158550), cells were incubated at a final concentration of 2.5 µM for 30 min at 37°C and 10% CO<sub>2</sub>. Then, live cells were stained with Hoechst 33342 (200 µg/mL for 10 min diluted in RPMI 1640 without phenol red supplemented with 1% FBS). Melanocytes were washed once with RPMI 1640 without phenol red, supplemented with 1% FBS, and imaged in the same medium. Images were acquired using the Operetta CLS™ High-Content Analysis System (PerkinElmer), with 63× Water/1.15 NA. Magic Red (excitation 530-560 nm; emission 600-640 nm), AO (excitation 450-490 nm; emission 590-650 nm).

**Transmission electron microscopy (TEM)**

8 x 10<sup>4</sup> melan-a/c2 cells per well were plated into 24-well plates. After 48h, cells were fixed, and sample preparation was performed as previously described. Samples were fixed with 2.5% glutaraldehyde in 0.1 M sodium cacodylate buffer, pH 7.4, O/N at 4°C. The samples were postfixed with 1% osmium tetroxide plus potassium ferrocyanide 1% in 0.1 M sodium cacodylate buffer for 1 h at 4°C. After three water washes, samples were dehydrated in a graded ethanol series and embedded in an epoxy resin (Sigma-Aldrich). Ultrathin sections (60-70 nm) were obtained with Leica Ultracut EM UC7 ultramicrotome, counterstained with uranyl acetate and lead citrate, and viewed with Tecnai G2 (FEI) transmission electron microscope operating at 100 kV. Images

were captured with a Veleta (Olympus Soft Imaging System) digital camera. TEM images and experiments were performed at the Electron Microscopy Facility of the University of Padua.

The TEM images and experiments were performed by the University of Padua electron microscopy facility. Mitochondria-melanosome distances and perimeters were quantified with the ImageJ (National Institutes of Health). At least four biological replicates were performed per cell line, with a minimum of five cells collected from each sample. The surface of every cell was completely covered by different images. The melanosome-mitochondria contact coefficient (MELAMICC) was used to represent the extent of physical interaction between the melanosome and mitochondria. This index considered the melanosome and mitochondria perimeter and the respective distance between the two organelles. Contacts with distances between organelle surfaces bigger than 120 nm were excluded. The MMERF was pre-embedded in 3% LMP agarose in 0.1 M cacodylate buffer and processed following the standard EM cell protocol.

### Statistical Analysis

Unless otherwise stated, data are presented as mean  $\pm$  SEM. All independent experiments represent biological replicates. Unless otherwise indicated, all experiments were performed at least three times. The statistical tests used are specified in the corresponding figure legends. Statistical significance was defined as \* $p < 0.05$ , \*\* $p < 0.01$ , \*\*\* $p < 0.001$ , and \*\*\*\* $p < 0.0001$ .

**Data Availability.** The MS data generated in this study have been deposited in the ProteomeXchange database with the identifier PXD051372 [<https://www.ebi.ac.uk/pride/archive/projects/PXD051372>]. Raw reads have been deposited in the NCBI SRA database and are available through the Bioproject ID PRJNA1092600 [<https://www.ncbi.nlm.nih.gov/bioproject/?term=PRJNA1092600>]. Raw files from imaging

experiments will be available on request. The processed data and W.blot images generated in this study are provided in the Supplementary Information/Source Data file. The unpublished melan-c2 cells, as well as the wild type cells melan-a will be readily available on request from the Functional Genomics Cell Bank at City St. George's, University of London, UK.

ARTICLE IN PRESS

## References

- 1 Bowman, S. L., Bi-Karchin, J., Le, L. & Marks, M. S. The road to lysosome-related organelles: Insights from Hermansky-Pudlak syndrome and other rare diseases. *Traffic* **20**, 404-435 (2019). <https://doi.org:10.1111/tra.12646>
- 2 Delevoye, C., Marks, M. S. & Raposo, G. Lysosome-related organelles as functional adaptations of the endolysosomal system. *Curr Opin Cell Biol* **59**, 147-158 (2019). <https://doi.org:10.1016/j.ceb.2019.05.003>
- 3 Ancans, J. *et al.* Melanosomal pH controls rate of melanogenesis, eumelanin/phaeomelanin ratio and melanosome maturation in melanocytes and melanoma cells. *Exp Cell Res* **268**, 26-35 (2001). <https://doi.org:10.1006/excr.2001.5251>
- 4 Diment, S., Eidelman, M., Rodriguez, G. M. & Orlow, S. J. Lysosomal hydrolases are present in melanosomes and are elevated in melanizing cells. *J Biol Chem* **270**, 4213-4215 (1995). <https://doi.org:10.1074/jbc.270.9.4213>
- 5 Zhou, B. K., Boissy, R. E., Pifko-Hirst, S., Moran, D. J. & Orlow, S. J. Lysosome-associated membrane protein-1 (LAMP-1) is the melanocyte vesicular membrane glycoprotein band II. *J Invest Dermatol* **100**, 110-114 (1993). <https://doi.org:10.1111/1523-1747.ep12462775>
- 6 Le, L., Sirés-Campos, J., Raposo, G., Delevoye, C. & Marks, M. S. Melanosome Biogenesis in the Pigmentation of Mammalian Skin. *Integr Comp Biol* **61**, 1517-1545 (2021). <https://doi.org:10.1093/icb/icab078>
- 7 Raposo, G., Tenza, D., Murphy, D. M., Berson, J. F. & Marks, M. S. Distinct protein sorting and localization to premelanosomes, melanosomes, and lysosomes in pigmented melanocytic cells. *J Cell Biol* **152**, 809-824 (2001). <https://doi.org:10.1083/jcb.152.4.809>
- 8 Van Den Bossche, K., Naeyaert, J. M. & Lambert, J. The quest for the mechanism of melanin transfer. *Traffic* **7**, 769-778 (2006). <https://doi.org:10.1111/j.1600-0854.2006.00425.x>
- 9 Bento-Lopes, L. *et al.* Melanin's Journey from Melanocytes to Keratinocytes: Uncovering the Molecular Mechanisms of Melanin Transfer and Processing. *Int J Mol Sci* **24** (2023). <https://doi.org:10.3390/ijms241411289>
- 10 Delevoye, C. *et al.* BLOC-1 Brings Together the Actin and Microtubule Cytoskeletons to Generate Recycling Endosomes. *Curr Biol* **26**, 1-13 (2016). <https://doi.org:10.1016/j.cub.2015.11.020>
- 11 Dennis, M. K. *et al.* BLOC-1 and BLOC-3 regulate VAMP7 cycling to and from melanosomes via distinct tubular transport carriers. *J Cell Biol* **214**, 293-308 (2016). <https://doi.org:10.1083/jcb.201605090>
- 12 Setty, S. R. *et al.* BLOC-1 is required for cargo-specific sorting from vacuolar early endosomes toward lysosome-related organelles. *Mol Biol Cell* **18**, 768-780 (2007). <https://doi.org:10.1091/mbc.e06-12-1066>
- 13 Sitaram, A. *et al.* Differential recognition of a dileucine-based sorting signal by AP-1 and AP-3 reveals a requirement for both BLOC-1 and AP-3 in delivery of OCA2 to melanosomes. *Mol Biol Cell* **23**, 3178-3192 (2012). <https://doi.org:10.1091/mbc.E11-06-0509>
- 14 Derivery, E. *et al.* The Arp2/3 activator WASH controls the fission of endosomes through a large multiprotein complex. *Dev Cell* **17**, 712-723 (2009). <https://doi.org:10.1016/j.devcel.2009.09.010>
- 15 Ripoll, L. *et al.* Myosin VI and branched actin filaments mediate membrane constriction and fission of melanosomal tubule carriers. *J Cell Biol* **217**, 2709-2726 (2018). <https://doi.org:10.1083/jcb.201709055>
- 16 Nag, S. *et al.* Rab4A organizes endosomal domains for sorting cargo to lysosome-related organelles. *J Cell Sci* **131** (2018). <https://doi.org:10.1242/jcs.216226>
- 17 Bissig, C. *et al.* The PIKfyve complex regulates the early melanosome homeostasis required for physiological amyloid formation. *J Cell Sci* **132** (2019). <https://doi.org:10.1242/jcs.229500>
- 18 Zhang, Z., Gong, J., Sviderskaya, E. V., Wei, A. & Li, W. Mitochondrial NCKX5 regulates melanosomal biogenesis and pigment production. *J Cell Sci* **132** (2019). <https://doi.org:10.1242/jcs.232009>
- 19 Daniele, T. *et al.* Mitochondria and melanosomes establish physical contacts modulated by Mfn2 and involved in organelle biogenesis. *Curr Biol* **24**, 393-403 (2014). <https://doi.org:10.1016/j.cub.2014.01.007>
- 20 Wang, J., Gong, J., Wang, Q., Tang, T. & Li, W. VDAC1 negatively regulates melanogenesis through the Ca(2+)-calcineurin-CRTC1-MITF pathway. *Life Sci Alliance* **5** (2022). <https://doi.org:10.26508/lsa.202101350>
- 21 Konig, T. *et al.* MIROs and DRP1 drive mitochondrial-derived vesicle biogenesis and promote quality control. *Nat Cell Biol* **23**, 1271-1286 (2021). <https://doi.org:10.1038/s41556-021-00798-4>
- 22 Bajpai, V. K. *et al.* A genome-wide genetic screen uncovers determinants of human pigmentation. *Science* **381**, eade6289 (2023). <https://doi.org:doi:10.1126/science.ade6289>

- 23 Parikh, R. *et al.* Recycled melanoma-secreted melanosomes regulate tumor-associated macrophage  
diversification. *Embo j* **43**, 3553-3586 (2024). <https://doi.org/10.1038/s44318-024-00103-7>
- 24 Otera, H. *et al.* Mff is an essential factor for mitochondrial recruitment of Drp1 during mitochondrial fission  
in mammalian cells. *J Cell Biol* **191**, 1141-1158 (2010). <https://doi.org/10.1083/jcb.201007152>
- 25 Passmore, J. B. *et al.* Mitochondrial fission factor (MFF) is a critical regulator of peroxisome maturation.  
*Biochim Biophys Acta Mol Cell Res* **1867**, 118709 (2020). <https://doi.org/10.1016/j.bbamcr.2020.118709>
- 26 Friedman, J. R. *et al.* ER tubules mark sites of mitochondrial division. *Science* **334**, 358-362 (2011).  
<https://doi.org/10.1126/science.1207385>
- 27 Ji, W. K. *et al.* Receptor-mediated Drp1 oligomerization on endoplasmic reticulum. *J Cell Biol* **216**, 4123-  
4139 (2017). <https://doi.org/10.1083/jcb.201610057>
- 28 Yasumoto, K. *et al.* Epitope mapping of the melanosomal matrix protein gp100 (PMEL17): rapid processing  
in the endoplasmic reticulum and glycosylation in the early Golgi compartment. *J Biol Chem* **279**, 28330-  
28338 (2004). <https://doi.org/10.1074/jbc.M401269200>
- 29 Kleele, T. *et al.* Distinct fission signatures predict mitochondrial degradation or biogenesis. *Nature* **593**, 435-  
439 (2021). <https://doi.org/10.1038/s41586-021-03510-6>
- 30 Adelman, C. H. *et al.* MFS12 mediates the import of cysteine into melanosomes and lysosomes. *Nature*  
**588**, 699-704 (2020). <https://doi.org/10.1038/s41586-020-2937-x>
- 31 Figon, F. *et al.* Catabolism of lysosome-related organelles in color-changing spiders supports intracellular  
turnover of pigments. *Proc Natl Acad Sci U S A* **118** (2021). <https://doi.org/10.1073/pnas.2103020118>
- 32 Borovanský, J. & Elleder, M. Melanosome degradation: fact or fiction. *Pigment Cell Res* **16**, 280-286 (2003).  
<https://doi.org/10.1034/j.1600-0749.2003.00040.x>
- 33 Goley, E. D. & Welch, M. D. The ARP2/3 complex: an actin nucleator comes of age. *Nature Reviews*  
*Molecular Cell Biology* **7**, 713-726 (2006). <https://doi.org/10.1038/nrm2026>
- 34 Jo, C. S. *et al.* A novel function of Prohibitin on melanosome transport in melanocytes. *Theranostics* **10**,  
3880-3891 (2020). <https://doi.org/10.7150/thno.41383>
- 35 Liu, A., Kage, F. & Higgs, H. N. Mff oligomerization is required for Drp1 activation and synergy with actin  
filaments during mitochondrial division. *Mol Biol Cell* **32**, ar5 (2021). <https://doi.org/10.1091/mbc.E21-04-0224>
- 36 Manor, U. *et al.* A mitochondria-anchored isoform of the actin-nucleating spire protein regulates  
mitochondrial division. *eLife* **4** (2015). <https://doi.org/10.7554/eLife.08828>
- 37 Derivery, E., Helfer, E., Henriot, V. & Gautreau, A. Actin polymerization controls the organization of WASH  
domains at the surface of endosomes. *PLoS one* **7**, e39774 (2012).  
<https://doi.org/10.1371/journal.pone.0039774>
- 38 Zhao, H. *et al.* On the analysis of the pathophysiology of Chediak-Higashi syndrome. Defects expressed by  
cultured melanocytes. *Lab Invest* **71**, 25-34 (1994).
- 39 O'Donnell, F. E., Jr., Hambrick, G. W., Jr., Green, W. R., Iliff, W. J. & Stone, D. L. X-linked ocular albinism. An  
oculocutaneous macromelanosomal disorder. *Arch Ophthalmol* **94**, 1883-1892 (1976).  
<https://doi.org/10.1001/archoph.1976.03910040593001>
- 40 Palmisano, I. *et al.* The ocular albinism type 1 protein, an intracellular G protein-coupled receptor, regulates  
melanosome transport in pigment cells. *Hum Mol Genet* **17**, 3487-3501 (2008).  
<https://doi.org/10.1093/hmg/ddn241>
- 41 Slominski, R. M. *et al.* Melanoma, Melanin, and Melanogenesis: The Yin and Yang Relationship. *Front Oncol*  
**12**, 842496 (2022). <https://doi.org/10.3389/fonc.2022.842496>
- 42 Bennett, D. C., Cooper, P. J. & Hart, I. R. A line of non-tumorigenic mouse melanocytes, syngeneic with the  
B16 melanoma and requiring a tumour promoter for growth. *Int J Cancer* **39**, 414-418 (1987).  
<https://doi.org/10.1002/ijc.2910390324>
- 43 Michalski, A. *et al.* Mass spectrometry-based proteomics using Q Exactive, a high-performance benchtop  
quadrupole Orbitrap mass spectrometer. *Mol Cell Proteomics* **10**, M111.011015 (2011).  
<https://doi.org/10.1074/mcp.M111.011015>
- 44 Perez-Riverol, Y. *et al.* The PRIDE database resources in 2022: a hub for mass spectrometry-based  
proteomics evidences. *Nucleic Acids Res* **50**, D543-d552 (2022). <https://doi.org/10.1093/nar/gkab1038>
- 45 Ewels, P., Magnusson, M., Lundin, S. & Källér, M. MultiQC: summarize analysis results for multiple tools and  
samples in a single report. *Bioinformatics* **32**, 3047-3048 (2016).  
<https://doi.org/10.1093/bioinformatics/btw354>

- 46 Chen, S., Zhou, Y., Chen, Y. & Gu, J. fastp: an ultra-fast all-in-one FASTQ preprocessor. *Bioinformatics* **34**, i884-i890 (2018). <https://doi.org:10.1093/bioinformatics/bty560>
- 47 Patro, R., Duggal, G., Love, M. I., Irizarry, R. A. & Kingsford, C. Salmon provides fast and bias-aware quantification of transcript expression. *Nature Methods* **14**, 417-419 (2017). <https://doi.org:10.1038/nmeth.4197>
- 48 Robinson, M. D., McCarthy, D. J. & Smyth, G. K. edgeR: a Bioconductor package for differential expression analysis of digital gene expression data. *Bioinformatics* **26**, 139-140 (2009). <https://doi.org:10.1093/bioinformatics/btp616>
- 49 Ashburner, M. *et al.* Gene Ontology: tool for the unification of biology. *Nature Genetics* **25**, 25-29 (2000). <https://doi.org:10.1038/75556>
- 50 Falcon, S. & Gentleman, R. in *Bioconductor Case Studies* 207-220 (Springer New York, 2008).
- 51 Timmons, J. A., Szkop, K. J. & Gallagher, I. J. Multiple sources of bias confound functional enrichment analysis of global -omics data. *Genome Biology* **16**, 186 (2015). <https://doi.org:10.1186/s13059-015-0761-7>
- 52 Nagashima, S. *et al.* Golgi-derived PI(4)P-containing vesicles drive late steps of mitochondrial division. *Science* **367**, 1366-1371 (2020). <https://doi.org:10.1126/science.aax6089>
- 53 Schindelin, J. *et al.* Fiji: an open-source platform for biological-image analysis. *Nat Methods* **9**, 676-682 (2012). <https://doi.org:10.1038/nmeth.2019>
- 54 Bolte, S. & Cordelières, F. P. A guided tour into subcellular colocalization analysis in light microscopy. *J Microsc* **224**, 213-232 (2006). <https://doi.org:10.1111/j.1365-2818.2006.01706.x>
- 55 Ge, S. X., Jung, D. & Yao, R. ShinyGO: a graphical gene-set enrichment tool for animals and plants. *Bioinformatics* **36**, 2628-2629 (2019). <https://doi.org:10.1093/bioinformatics/btz931>

## Acknowledgments

We thank all members of the Dibio Imaging facility (<https://www.biologia.unipd.it/servizi/servizi-alla-ricerca/imaging-facility/>) for technical assistance on sample preparation and image acquisition. Sequencing services were performed by the NGS facility of the Department of Biology, Univ. of Padua.

This work was supported by the following grants: LEO Foundation Open Competition grant LF-OC-20-000630 (M.G.), LEO Foundation Serendipity grant LF-SE-23-800010 (M.G.) and Wellcome Trust grant 108429/Z/15/Z (E.V.S.).

## Authors Contribution Statement

Conceptualization: APMR, MGi

Methodology: APMR, AM, AP, FDB, MGe, MGi, SG, SS

Formal analysis: APMR, SG, LSa, MGe, PGru

Investigation: APMR, AM, PGru, TK

Resources: EVS, PGoff, LSc, MGi, CF

Data curation: APMR, SG, LSa

Writing—original draft: APMR, MGi

Writing—review and editing: all authors

Supervision: MGi

Funding acquisition: MGi, EVS

**Competing Interest Statement:** Authors declare that they have no competing interests.

**Figure 1. MFF is a new candidate for melanosome function.**

(A) Representative TEM images of melan-a and melan-c2 cells showing melanosomes at different maturation stages (MLI–MLIV). Scale bar, 1  $\mu$ m. (B) Quantification of the percentage (%) of melanosomes at each maturation stage in contact with mitochondria. Data are expressed as the % of total melanosomes contacting mitochondria per replicate. Mean  $\pm$  SEM from four independent experiments. One-way ANOVA, \* $p$  = 0.0189. (C) Quantification of the Melanosome–Mitochondria Contact Coefficient (MELAMICC), calculated as the melanosome perimeter divided by the product of mitochondrial perimeter and melanosome–mitochondria distance. Mean  $\pm$  SEM from four independent experiments (MLI vs MLII \* $p$  = 0.0217; MLI vs MLIII  $p$  = 0.079; MLI vs MLIV \*\* $p$  = 0.0073 and melan-a MLI vs melan-c2 MLI \* $p$  = 0.0015; one-way ANOVA). (D) David GO cellular component enrichment analysis of the DEGs between melan-a and melan-c2. Enrichment significance was determined using the EASE (modified Fisher’s exact) test with Bonferroni correction,  $p$ -value < 0.05. Blue and red bars represent upregulated DEGs in melan-a and melan-c2, respectively. (E) Heatmap of mitochondrial-related DEGs ( $n$  = 531) based on MitoCarta3.0 analysis. Upregulated genes are shown in red and downregulated genes in blue. Representative of three independent experiments. (F) Schematic of mitochondria–melanosome–ER fraction (MMERF) isolation, proteinase K treatment, and Mass Spectrometry analysis (MS; four independent experiments). (G) Representative TEM images of total and magnified views of mitochondria contact sites with melanosomes (arrows) from MMERFs from three independent experiments. Scale bar, 1  $\mu$ m. (H) Proteomic analysis of MMERFs identifying common ( $n$  = 109) and cell line–specific proteins (melan-a,  $n$  = 136; melan-c2,  $n$  = 242), followed by DAVID GO cellular component enrichment analysis (Bonferroni  $p$  < 0.05). Outer mitochondrial membrane (OMM), endoplasmic reticulum (ER), and Golgi apparatus (Golgi). OMM proteins that were also detected as DEGs are highlighted (blue, melan-a; red, melan-c2). (I) SR time-lapse images of

melan-a and melan-c2 stained with lysotracker and mitotracker showing melanosomal fission events (red arrows). Scale bar 1 $\mu$ m. **(J, K)** Quantification of the number of Lysotracker spot fission events and their perimeter per cell; three independent experiment, n = 6-8 cells each. Mean  $\pm$  SEM, two-tailed unpaired Student's t-test, \*\*\*\*p < 0.0001. **(L)** Representative immunoblot validation of MMERFs showing enrichment of MFF in melan-c2 cells of three independent experiments.

**Figure 2. MFF locates at melanosomes and associates with melanosome fission sites.**

**(A)** Immunogold labeling of MFF and HMB45 reveals the presence of MFF at all melanosome maturation stages. Representative images of two biological replicates. **(B, C)** Pigmented (melan-a) and albino (melan c2) melanocytes were stained with anti-MFF, HMB45, and LAMP1 antibodies. White arrows show MFF association with HMB45-positive structures, both in melan-a and melan-c2. Single plane images; scale bar, 1  $\mu$ m. Representative images of three biological replicates. **(D, E)** Linescans of the relative fluorescence intensity of MFF (green), HMB45 (magenta), and LAMP1 (red) of the white lines reported in B and C, respectively. **(F)** Quantification of the number of HMB45-positive melanosomes with MFF puncta ( % of total melanosomes) in melan-a cells. Mean  $\pm$  SEM; n= 20 cells, two independent experiments; for each cell, two to four ROIs were randomly selected. **(G)** Colocalization analysis shows decreased colocalization of MFF with mitochondria (mt-RFP) in albino melanocytes. Mean  $\pm$  SEM; n=10 cells from two independent experiments (three ROIs per cell). Two-tailed Mann-Whitney test, \*\*\*p < 0.0004. **(H)** SRimages of melanosomes with membrane fission regions and vesicle/tubule formation in association with MFF punctae. Scale bar 1 $\mu$ m. **(I)** Quantification of MFF colocalization with melanosomal fission events per ROI (% of total fission regions). Mean  $\pm$  SEM; n= 20 cells from two independent experiments; for each cell, two to four ROIs were randomly

selected. **(J)** Representative time-lapse images of MFF budding from mitochondria to melanosomes (LAMP1-RFP structures). White arrows indicate the event. Scale bar 1 $\mu$ m. **(K)** SR time-lapse images of melan-a cells co-expressing eGFP-MFF isoform 1 and LAMP1-RFP. White arrows indicate melanosome sites where MFF is associated with constricted membranes that undergo fission. Scale bar 1 $\mu$ m.

**Figure 3. MFF modulates melanosome function and morphology.**

**(A)** Representative SR images of MFF, DRP1, and melanosomes (LAMP1). Scale bar 2 $\mu$ m and 1 $\mu$ m in the magnified ROIs (A and B). Orange arrows point to MFF and DRP1 colocalization in mitochondria, while white (MFF) and yellow (DRP1) arrows indicate the presence of these proteins in melanosomal structures (LAMP1 positive). Representative images of two independent experiments. **(B)** Representative Western Blotting image showing MFF and Drp1 silencing in melan-a cells, and expression levels of melanogenesis-related proteins of five biological replicates. **(C)** Representative SR images of HMB45 immunostaining in melan-a cells under the indicated silencing conditions. Scale bar 2  $\mu$ m. Red arrows highlight melanosomes with different morphology. **(D, E)** Quantification of melanosome number and perimeter (n = 4083 cells for control siRNA; n = 42597 cells for Mff siRNA; n = 3846 cells for Drp1 siRNA; n=4 independent experiments; px = pixel). Mean $\pm$  SEM. Kruskal–Wallis test followed by Dunn’s multiple comparisons test, \*p = 0.0194. **(F)** Representative TEM images of stage I and stage II melanosomes with dysfunctional morphology and lumen buildup in MFF-silenced melan-a compared to control from three biological replicates. Scale bar 1  $\mu$ m. **(G)** Live-cell imaging sequence showing mitochondria (Mitotracker, green) and an elongated melanosomal structure (LAMP1-RFP, magenta) that does not successfully undergo fission (white arrows) in Mff-silenced cells. Scale bar 1  $\mu$ m. **(H)** The fission of melanosomes was observed using time-lapse imaging in both control and MFF-silenced melan-a cells. The number of fission events per cell is shown. n=20

cells from three independent experiments. Mean  $\pm$  SEM; two-tailed unpaired Student's t-test, \*p = 0.0457. **(I)** Representative images of MFF-silenced melanocytes with HMB45 immunostaining: the insets show an increased colocalization of HMB45-positive organelles with melanosomes that are enriched in melanin, as seen in brightfield (BF) images. Scale bar 2  $\mu$ m. **(J)** HMB45 colocalization with melanin was quantified from confocal images of the respective conditions. Mean  $\pm$  SEM; n=40 cells from four independent experiments. Two-tailed Mann-Whitney test, \*p = 0.0411.

**Figure 4. CTSB upregulation in response to MFF silencing enhances catabolism in melanosomal lumen**

**(A)** Gene ontology analysis (ShinyGO online tool <sup>S55</sup>) of genes changed upon *Mff* and *Drp1* silencing in melan-a; three independent experiments. MFF, but not DRP1, silencing induces lysosomal and catabolism pathways in melanocytes. **(B)** Representative Western Blotting image of CTSB expression in melan-a treated with *Mff*, *Drp1*, and control siRNA. **(C)** Quantification of CTSB expression levels in silenced melan-a, normalized to  $\beta$ -actin. Mean  $\pm$  SEM; from four independent biological experiments. Kruskal–Wallis test followed by Dunn's multiple comparisons test, \*p = 0.0252. **(D)** Representative images of control and *Mff* siRNA-treated melanocytes stained with HMB45 and anti-CTSB antibody. Scale bar, 10  $\mu$ m, and for magnified regions, 1  $\mu$ m. **(E)** Quantification of HMB45 colocalization with CTSB in melan-a melanocytes treated with control and MFF siRNA. Mean  $\pm$  SEM; n=30 cells from three independent experiments. Two-tailed Mann-Whitney test, \*p = 0.0189. **(F)** Representative images of the Magic Red assay for the measurement of CTSB degradative activity in control and *Mff*-silenced melan-a. Scale bar 200  $\mu$ m. **(G)** Quantification of CTSB activity (Magic Red intensity, a.u. = arbitrary

units) in *Mff*-silenced melan-a. Mean  $\pm$  SEM; four independent experiments. Two-tailed Mann-Whitney test, \* $p = 0.0286$ . **(H)** Representative images of melan-a stained with Acridine Orange (AO) and treated with the indicated siRNA. AO-positive spots were detected by automated image analysis (Harmony® software). Scale bar 100  $\mu$ m. **(I)** Quantification of AO intensity in melan-a treated with the indicated siRNA. Mean  $\pm$  SEM, four independent experiments. Kruskal–Wallis test followed by Dunn’s multiple comparisons test, \* $p = 0.0407$ . **(J)** Representative Western Blotting image of control and double silencing of *Mff* and *Ctsb* in melan-a. **(K)** Automated detection and analysis (Harmony® software) of HMB45-positive melanosomes was applied for quantification of their perimeter in melan-a cells treated with *Mff* and *Ctsb* siRNA. Mean  $\pm$  SEM, four independent experiments. Two-tailed unpaired Student’s t-test, \* $p = 0.0274$ . **(L)** Quantification of melanosome number in *Mff* and *Ctsb*-silenced melan-a cells. Mean  $\pm$  SEM, four independent experiments. Two-tailed unpaired Student’s t-test. \* $p = 0.0274$ .

**Figure 5. MFF-dependent melanosome fission is dependent on F-actin nucleation by interaction with ARP2/3 complex regulators.**

**(A)** Proteomic analysis of MFF interactome: scatter plot shows the distribution of MFF interactors according to the levels of protein difference (x-axis) and statistical significance (y-axis). Magenta dots represent the statistically significant deregulated proteins, respectively. MFF is visualized in the upper right corner of the graph as the most upregulated protein. Cyan dots highlight proteins belonging to the WASH complex (FAM21C and Strumpellin (Kiaa0196)). Two-tailed Student t-test analysis was applied, and significance  $p < 0.05$ . **(B)** Representative Western Blot of MFF co-immunoprecipitation with FAM21C and Strumpellin of two independent experiments. **(C)** Gene ontology (biological process) enrichment of the MFF-IP proteome shows high enrichment of proteins involved in the regulation of ARP2/3 complex-mediated actin nucleation. **(D)** Representative SR images of MFF, HMB45, and phalloidin (F-actin) immunostaining in melan-a

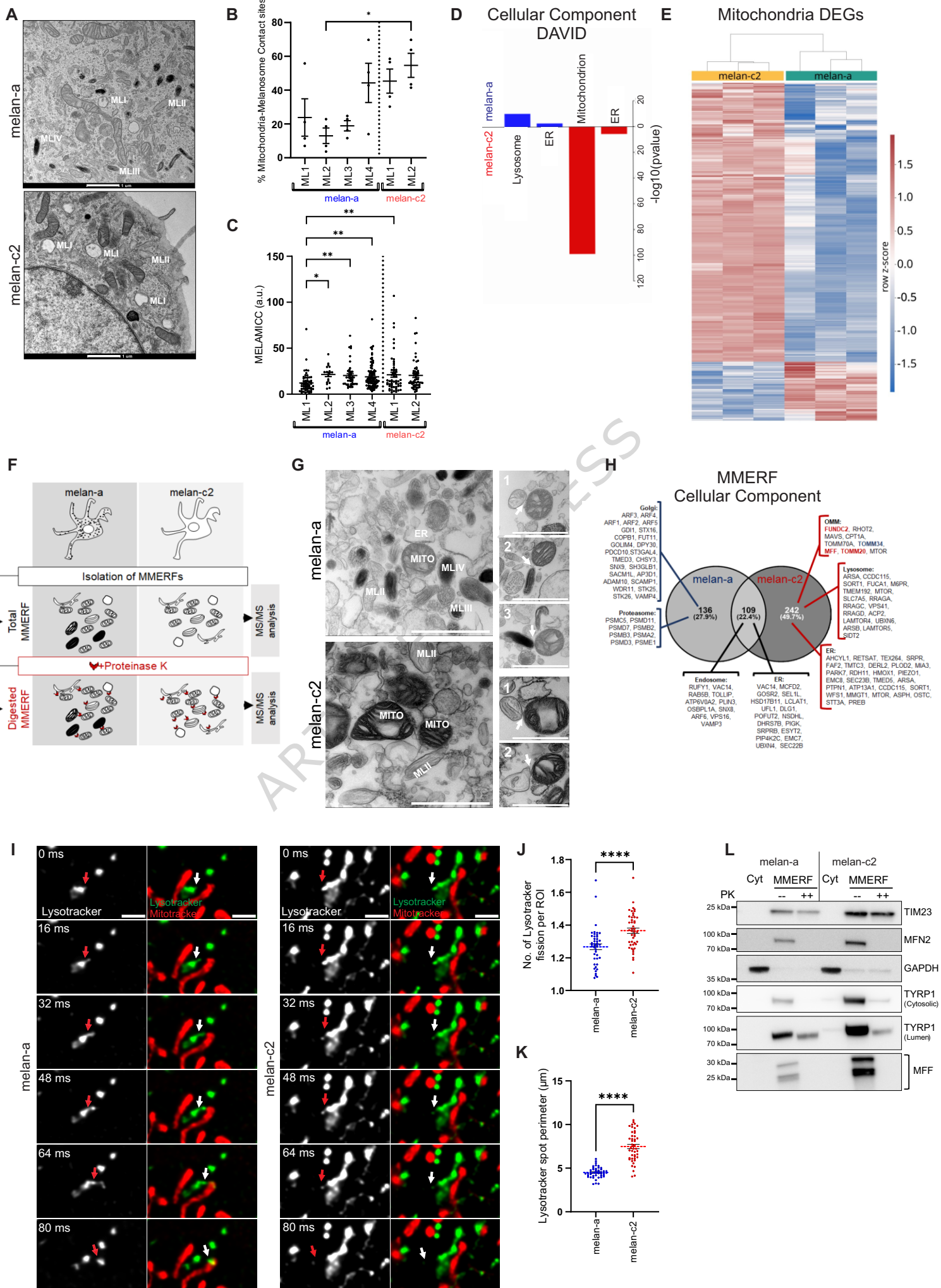
cells. The white line indicates the enrichment of F-actin at the MFF puncta in HMB45 melanosomes (panel 1) and melanosome constriction sites (panel 2). Scale bar 1  $\mu\text{m}$ . **(E)** Linescans of the relative fluorescence intensity of MFF (green), HMB45 (magenta), and phalloidin (grey) of the white lines drawn in panels 1 and 2 (Fig. 5D). **(F)** Representative SR images showing eGFP-MFF colocalization with ARP2/3 at melanosomes and melanosome membrane constriction regions (white arrows). Scale bar 1  $\mu\text{m}$ . **(G)** HMB45-positive melanosome volume was quantified in control and *Arpc1A*- or *Arpc3*-silenced melan-a cells. Mean  $\pm$  SEM; n= 29 cells for siRNA control and siRNA *Arpc3*, n=27 cells for siRNA *Arpc1A*, from three independent experiments, px=pixel. Kruskal–Wallis test followed by Dunn’s multiple comparisons test, \*\*\*\*p=0.0001. Scale bar 1  $\mu\text{m}$ . **(H)** Quantification of the melanosomes perimeter in melan-a treated with control and *Mff* siRNA, along with the ARP2/3 inhibitor CK-666. Cells were treated with DMSO or 50  $\mu\text{M}$  CK-666 for 30 minutes. Mean  $\pm$  SEM, three independent experiments. Kruskal–Wallis test followed by Dunn’s multiple comparisons test, \*p = 0.0485.

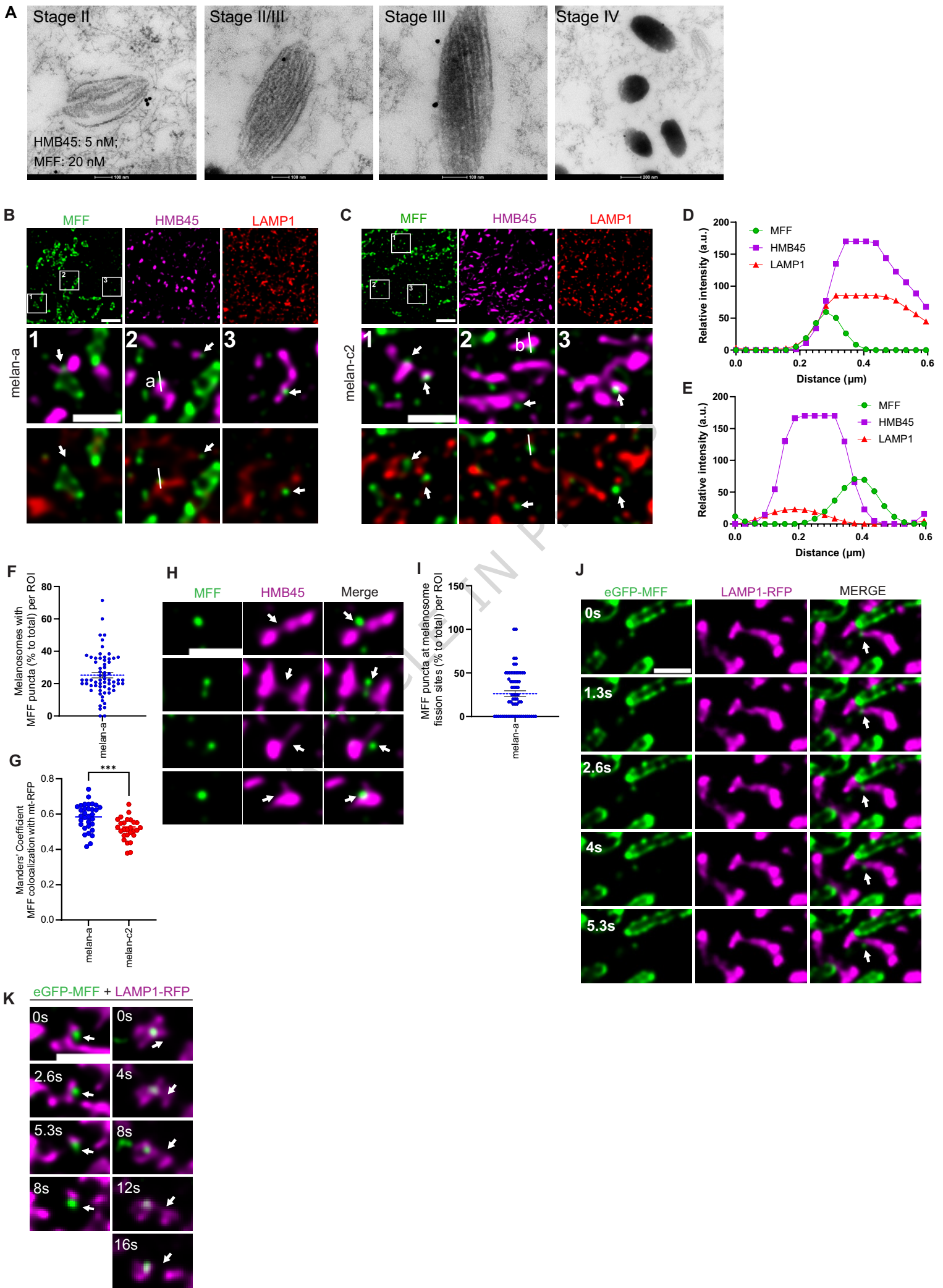
**Editor's****Summary:**

Melanosome maturation depends on poorly understood fission processes. Here, the authors demonstrate that the mitochondrial fission factor MFF mediates melanosome division by localising to division sites, trafficking between mitochondria and melanosomes and regulating ARP2/3-dependent actin assembly.

**Peer review information:** *Nature Communications* thanks Duarte Barral, Qing Deng and the other, anonymous, reviewer(s) for their contribution to the peer review of this work. A peer review file is available.

ARTICLE IN PRESS







Go Enrichment  
Cellular Component